Chemical Engineering Journal Advances 22 (2025) 100721

Contents lists available at ScienceDirect

Chemical Engineering Journal Advances

journal homepage: www.sciencedirect.com/journal/chemical-engineering-journal-advances

Simultaneous removal of multiple organic micropollutants via UV-visible light driven $BiVO_4/TiO_2$-GO photoanode: Experimental and CFD study

Agha Zeeshan Ali [a,*], Yuhao Wu [b], Bas Wols [c,d], Mohamad Zeidan [c], Henri Spanjers [a], Jan Peter van der Hoek [a,e]

[a] Department of Water Management, Faculty of Civil Engineering and Geosciences, Delft University of Technology, P.O Box 5048, 2600 GA Delft, the Netherlands
[b] Department of Civil and Mineral Engineering, University of Toronto, Toronto, ON M5S 1A4, Canada
[c] KWR Water Research Institute, 3433 PE, Nieuwegein, the Netherlands
[d] Wetsus Research Institute, 8911 MA Leeuwarden, the Netherlands
[e] Waternet, department of Research & Innovation, P.O. Box 94370, 1090 GJ Amsterdam, the Netherlands

ARTICLE INFO

Keywords:
Photoelectrocatalysis
Advanced oxidation process
Heterojunction photoanode
Bismuth vanadate
Organic micro-pollutants
Computational fluid dynamics model

ABSTRACT

In this study, we investigated the use of $BiVO_4/TiO_2$-GO heterojunction photoanode in a PEC based AOP to simultaneously remove four organic micropollutants (OMPs): benzotriazole (BTA), carbamazepine (CBZ), caffeine (CAF) and diclofenac (DIC) from demineralized water. Each OMP had an initial concentration of 40 μg L^{-1}. Ultrasonic spray pyrolysis (USP) was used to deposit $BiVO_4$ and TiO_2-GO layers on fluorine doped tin oxide (FTO) electrodes. The heterojunction photoanode at an applied voltage of 1 V (vs Ag/AgCl) achieved simultaneous removal efficiencies of 100 % for DIC, 54 % for CBZ, 36 % for BTA and 33 % for BTA under simulated solar light. Compared to the pristine $BiVO_4$ photoanode, the heterojunction photoanode showed 50 % higher removal efficiency for BTA, CBZ and CAF. The reaction kinetics revealed that the first order rate coefficient for DIC removal was about nine times higher than that of CBZ and fifteen times higher than those of BTA and CAF. To assess scalability, a computational fluid dynamics (CFD) model incorporating the experimentally determined reaction kinetics was developed for a conceptually designed up-scaled PEC reactor. The model analyzed the effect of reactor design and fluid flow conditions on the removal of OMPs. Under turbulent flow conditions, enhanced removal efficiency was observed for all four OMPs, which was attributed to the effects of eddy diffusion and convective mixing. The optimized reactor design under turbulent flow condition achieved an 80 % removal efficiency for all four OMPs within 25 min under a light intensity of 400 W m^{-2}. The findings highlight the potential of $BiVO_4/TiO_2$-GO heterojunction photoanodes for efficient and scalable PEC water treatment, showing a promising approach for the elimination of OMPs from wastewater.

1. Introduction

Organic micropollutants (OMPs) belong to an expanding range of organic pollutants that are present in water bodies due to industrial and human activities [1]. OMPs consist of a variety of organic compounds, which include pharmaceutical drugs, corrosion inhibitors, pesticides, surfactants and personal care products [2]. Depending on the geographical location and source of origin, OMPs are typically present within the range of ng L^{-1} and μg L^{-1} in the surface water [3]. Industrial and municipal wastewater treatment plant (WWTP) effluents are becoming a major contributor to the release of OMPs in the surface water [4]. Conventional wastewater treatment technologies are ineffective to completely remove OMPs from the wastewater [5], therefore, research efforts are increasing to enhance the existing technologies to remove OMPs or to convert them into less harmful compounds.

Advanced oxidation processes (AOPs) and related technologies are effective for eliminating OMPs from industrial and municipal WWTP effluents [6,7]. Different AOPs such as ozonation [8], electrochemical oxidation [9], persulfate oxidation [10] and Fenton reactions [11] have been studied in the literature for the removal of organic pollutants (primarily pharmaceuticals) from aqueous solutions. However, these processes have several disadvantages including high power consumption, high chemical cost (particularly in persulfate oxidation, which

* Corresponding author.
E-mail address: a.aghazeeshan@tudelft.nl (A.Z. Ali).

https://doi.org/10.1016/j.ceja.2025.100721

Available online 24 February 2025

requires a continuous supply of persulfate salts), short lifetime of reactive species, incomplete mineralization of pollutants leading to the formation of toxic byproducts, and pH dependency (as observed in both ozonation and Fenton reactions) [12]. Photoelectrocatalytic (PEC) based AOP is in its early stage of development. In PEC-based AOPs, semiconducting photocatalytic materials are used as anodes, facilitating the generation of hydroxyl radicals (•OH) and superoxide radicals ($^{\bullet}O_2^-$) as primary oxidants in water [13]. The anode in a PEC cell, the photoanode, coated with a photocatalytic material is in direct contact with the water containing the OMPs, and the removal reaction usually takes place within the close vicinity of the anode-electrolyte interface [14]. When solar light interacts with the photoanode, electron-hole pairs are generated. The holes oxidize water molecules to form •OH, while the electrons reduce dissolved oxygen, yielding $^{\bullet}O_2^-$. These photoinduced •OH and $^{\bullet}O_2^-$ react with the OMP molecules through oxidative mechanisms and either completely oxidize them or convert them into less harmful products [13]. The main advantages of PEC based AOP over other AOPs are enhanced pollutant mineralization, lower energy consumption through the integration of solar energy, and efficient removal of emerging contaminants such as antibiotics and pesticides.

UV driven photocatalysts including titanium dioxide (TiO_2) [15], tungsten trioxide (WO_3) [16] and zinc oxide (ZnO) [17] have been extensively used for the removal of industrial dyes and pharmaceuticals (1–10 mg L^{-1}) in aqueous solution through PEC based AOP. A major drawback of using UV driven photocatalysts is that they have a wide band gap energy ranging from approximately 3.0 to 3.5 eV, which allows them to absorb only less than 10 % (180 – 400 nm) of the solar spectrum. Bismuth vanadate ($BiVO_4$), a photocatalyst activated by visible light, is emerging as an alternative to UV driven photocatalysts for PEC water treatment applications [18]. Studies have explored $BiVO_4$ based photoanodes for removing dyes and pharmaceuticals (concentrations ranging from 1 to 10 mg/L) from aqueous solutions via PEC based AOPs [19,20]. However, the effectiveness of $BiVO_4$ photoanodes is hindered by the rapid recombination of photoinduced holes and electrons, which limits charge transport to the anode surface and reduces the formation of •OH and $^{\bullet}O_2^-$ [21]. Applying a suitable external voltage to $BiVO_4$ photoanode is one of the ways to reduce the rate of recombination and ultimately increase its removal efficiency. Combining $BiVO_4$ with a different UV or visible light driven photocatalyst and thereby creating a heterojunction is also an effective way to reduce rate of recombination in $BiVO_4$. In heterojunction photoanode, the photo-generated holes and electrons are separated from each other by travelling in opposite direction within the photocatalytic layers and increasing their lifetime to produce •OH and $^{\bullet}O_2^-$ [22]. Graphene oxide (GO) is a photo active semi-conducting material with high specific area [23]. It is also used for water treatment applications either as a heterojunction photocatalyst with TiO_2 or mixed in the TiO_2 layer [24]. GO helps to increase the charge separation efficiency in heterojunction photoanodes and also increases the specific surface area for the adsorption of molecules of OMPs [23].

Benzotriazole (BTA) is a corrosion inhibitor mostly used in anti-icing fluids and dishwashing detergents [25]. Within the European Union, BTA is an emerging OMP that is frequently detected in surface water resources at concentrations ranging from 10 to 50 μg L^{-1} [26]. Due to its low biodegradability and weak adsorption to organic matter, BTA is only partially removed during biological treatment in WWTPs [26]. UV/H_2O_2 [27] and photocatalytic [28] based AOPs have been employed to remove BTA (1–10 mg L^{-1}) from WWTP effluents. Carbamazepine (CBZ) is an anticonvulsant medicine that is a frequently detected OMP in surface water and WWTP effluents [29]. CBZ is resilient to chlorination and UV photolysis based water treatment processes, which is why it is only partially removed from the wastewater [30]. As a result of its partial removal in a WWTP, CBZ is released into the surface water through the WWTP effluent discharge. UV/chlorine [31] and electrochemical based AOP [32] have been applied to remove CBZ (1–10 mg L^{-1}) from water. Caffeine (CAF) is a central nervous system stimulant that is extensively used to increase focus and reduce body fatigue [33]. CAF is also an emerging OMP in surface water resources because it is only partially removed by the conventional wastewater treatment technologies [34]. Chemical oxidation, ozonation [34] and photocatalytic based AOP [35] have been applied in some studies for the removal of CAF (5–50 mg L^{-1}) from water. Diclofenac (DIC) is an anti-inflammatory drug and it is frequently detected as an OMP in the aquatic environment [36]. It is only partially removed during conventional wastewater treatment due to its low biodegradability [37], hence it is also released in the environment through WWTP effluent. Adsorption and UV-A based treatment [38] have been used for the removal of DIC (10–50 mg L^{-1}) from water. A previous study conducted by the Dutch Ministry of Water and Infrastructure reported the presence of BTA, CBZ and DIC in WWTP effluents at concentrations below 5 μg L^{-1} [39]. The presence and accumulation of BTA, CBZ, CAF and DIC in the surface water will become a major threat to human health and aquatic life. To the best of our knowledge, there is no publication available on the simultaneous removal of BTA, CBZ, CAF and DIC from either demineralized water or WWTP effluent through PEC based AOP.

In this study, we investigated the application of $BiVO_4/TiO_2$-GO heterojunction photoanode for the simultaneous removal of BTA, CBZ, CAF and DIC from demineralized water. A starting concentration of 40 μg L^{-1} was used in this study because it was comparable to typical concentrations of the selected OMPs in surface water. Demineralized water was used in this study because it provided a controlled environment in which we could investigate the effect of photoanode on the removal kinetics. The treated wastewater effluent may contain ions that can inhibit the production of reactive species and interfere with the PEC based AOP removal, therefore, demineralized water was used to determine the effectiveness of $BiVO_4/TiO_2$-GO heterojunction photoanode for the removal of selected OMPs. Pristine $BiVO_4$ photoanodes and $BiVO_4/TiO_2$-GO photoanodes were fabricated by using ultrasonic spray pyrolysis (USP) method. The optical properties of fabricated photoanodes were analyzed to confirm the successful deposition of photocatalytic layers and the formation of heterojunctions, which enhance photocatalytic activity. The photoanodes, specifically fabricated for this research, were used in a three electrode PEC cell. The removal reaction rate coefficient (k) of each OMP was determined by applying a suitable reaction kinetics model. Then the rate coefficient of each OMP was used in computational fluid dynamic (CFD) model to assess the removal of BTA, CBZ, CAF and DIC in an up-scaled PEC water treatment reactor (shown in the supplementary information Fig. S. 1). CFD is a valuable tool for assessing the flow behaviour of water in wastewater treatment processes [40]. CFD models are also used for assessing the removal of organic pollutants through a photocatalytic reaction, however, most models are based on the removal of only one organic pollutant with a relatively high starting concentration (>10 mg L^{-1}) [41–43]. There is a lack of literature available on the CFD modelling of a PEC based AOP removal of multiple OMPs. This study used a novel approach of using CFD simulation for simultaneous removal of BTA, CBZ, CAF and DIC in a PEC water treatment reactor.

2. Materials and methods

2.1. $BiVO_4/TiO_2$-GO photoanode preparation

The $BiVO_4$ and TiO_2-GO photocatalytic layers were deposited on an FTO glass surface (40 mm x 40 mm, 7 Ω/square, Luoyang Guluo glass Co., Ltd., China) by ultrasonic spray pyrolysis (USP) method. The FTO glass was first ultra-sonicated in acetone for 5 mins and then rinsed with demineralized water to clean the surface. The spray precursor solution for $BiVO_4$ layer was prepared as follows. 0.02 M bismuth nitrate pentahydrate ($Bi(NO_3)_3{\cdot}5H_2O$ (99 % Sigma Aldrich)) was dissolved in 10 mL acetic acid (CH_3COOH (98 % Sigma Aldrich)) and an equimolar amount of vanadyl acetylacetonate ($VO(AcAc)_2$ (99 % Sigma Aldrich))

was dissolved in 20 mL demineralised 1:1 (v:v) water-ethanol mixture. The precursor solution was then made by mixing above solutions together slowly to form a clear blue homogenous solution. The spray coating process was carried out by an ultrasonic spray system (MSK-USP-ST1, MTI Corporation, USA). A multistage X-Y axis CNC controller was used in this system to control the progressive scanning motion of the nozzle using a set of programmed X–Y linear motion stages. The distance between the titanium alloy cylindrical spray nozzle and the substrate was 10 cm and the FTO substrate was kept at 300 °C on a hot plate (EQ-HP-1515-LD, MTI Corporation, USA) in an open atmosphere. The nozzle was fixed to a 0.05 W digital ultrasonic generator (MSK-SP-01A, MTI Corporation, USA) and the feeding rate of the precursor solution was set at 0.3 mL/h by a syringe pump (NE-1010, ProSense B.V., the Netherlands). The pressure of the compressed air acting as a carrier gas was fixed at 0.25 bar. The spray coating process was conducted twice to form the homogeneous nanostructured $BiVO_4$ film. Subsequently, the prepared $BiVO_4$ photoanodes were annealed at 460 °C for 2 h with a ramping rate of 2 °C per minute. To prepare the spray precursor solution for TiO_2-GO film on previously prepared $BiVO_4$ photoanodes, 0.001 M nano GO powder (Suzhou Tanfeng Graphene Technology Co., Ltd., China) was first dispersed in 30 mL demineralised 1:9 (v:v) water and ethanol mixture and ultra-sonicated for 1 h. Then 0.02 M P25 TiO_2 nano powder (Tianjin Baima Technology Co., Ltd., China) was added into the above mixture and then stirred for 2 h and ultra-sonicated again for 1 h. The spray coating method was the same as for the $BiVO_4$ film, except that the temperature of the heating plate was 150 °C. Finally, the prepared electrodes were annealed at 500 °C for 1 h in the oven with ramp rate of 5 °C per minute and used for further characterizations and degradation experiments.

2.2. Structural characterization

The phase composition of the fabricated photoanodes was identified using X-Ray diffraction (XRD) technique. A detailed description of the XRD parameter is provided in our previous publication [44].

2.3. Optical characterization

The absorbance spectra of the fabricated photoanodes were obtained between 300 and 700 nm (5 nm step size) by using diffusive reflectance UV–vis spectroscopy (The LAMBDA 1050+ UV/Vis/NIR spectrophotometer, UV Winlab software).

2.4. Photo-electrocatalytic (PEC) experiments

Photo-electrocatalytic (PEC) based simultaneous removal of four OMPs (BTA, CBZ, CAF and DIC) was carried out by using the prepared photoanodes in combination with a Autolab potentiostat (PGSTAT128N) in a three electrode configuration set-up. A quartz reactor cell containing three electrodes and 167 mL of electrolyte solution was used for the PEC experiments. A 0.1 M Na_2SO_4 solution was prepared with demineralized water and used as the electrolyte for the experiments. Each OMP was then added to the electrolyte to achieve a concentration of 40 μg L^{-1}. The starting pH of the electrolyte was set at 5.1 by adding 0.2 mL of 0.5 M nitric acid (HNO_3) to facilitate a higher in-situ production of hydroxyl radicals ($^{\bullet}OH$). The experimental setup included fabricated photoanodes as the working electrode, an Ag/AgCl (3.0 M KCl) electrode as the reference electrode, and a graphite plate (40×40 mm) as the counter electrode. During the removal experiments, a constant voltage of 1 V vs. Ag/AgCl was applied to reduce the recombination rate in the photoanodes. Solar simulator (SUNTEST XXL+) equipped with three air-cooled 1700 W Xenon lamps, which produced a light spectrum equivalent to 1 sun was used as the illumination source. The intensity of emitted light between 300 and 400 nm was 60 W/m^2 and the distance between the light source and the photoanode was 23 cm. During the experiments the reaction solution was constantly stirred at 600 rpm with the help of a magnetic stirrer to enhance the transport of OMPs molecules from the bulk towards the surface of the photoanode. During the Pec experiment, the temperature of the quartz reactor cell was maintained at 25 °C (±2 °C) by using a temperature controlling bath. Each experiment ran for 3 h and samples were taken at an interval of 30 min for the measurement of DIC, BTA, CAF and CBZ concentration. Photolysis experiments were conducted to investigate the simultaneous removal of OMPs in demineralized water as a result of direct irradiation in the absence of a photoanode. For the photolysis experiment, the total duration was 3 hr and the starting concentration of each OMP was 40 μg L^{-1} in demineralized water. Reusability experiments were conducted using a $BiVO_4/TiO_2$-GO heterojunction photoanode over three consecutive removal experiments of 3 hours each. Each OMP had an initial concentration of 40 μg L^{-1} in demineralized water. Between each experiment, the photoanode was rinsed with demineralized water to remove any adsorbed OMPs from its surface.

2.5. Analytical measurement of OMPs

The concentrations of OMPs in the samples were determined using liquid chromatography coupled with tandem triple quadrupole mass spectrometry (LC-MS). A Waters Acquity UPLC BEH C18 column was used for the analysis of BTA, CAF, CBZ, and DIC. Prior to analysis, all samples were filtered through 0.2 μm glass fiber filters (GF-75, ADVANTEC®, Japan). Subsequently, 495 μL of the filtered sample solution was combined with 5 μL of an internal standard calibration solution in LC-MS sample vials. After thorough mixing, the LC-MS system quantified the target compounds in the samples. The removal efficiency of the photoanodes, based on the concentrations of the target compounds, was determined using the following equation:

$$\text{Removal efficiency } (\%) = \left(1 - \frac{C_t}{C_0}\right) \times 100 \quad (1)$$

where C_0 = Initial concentration at time t=0 and C_t = Concentration at time t.

2.6. CFD modelling of photoelectrocatalytic (PEC) water treatment reactor

A CFD model was used to simulate a full-scale reactor by using the results from the lab-scale reactor cell discussed in Section 3.2. A conceptually designed photo-electrocatalytic water treatment reactor, as shown in Fig. S. 1 of the supplementary information, was used for the CFD simulation by using COMSOL multi-physics software. The reactor was conceptually designed to remove BTA, CBZ, CAF and DIC from water, with the target of at least 80 % removal. In this design, the water stored in a storage tank is pumped into the reactor, where the photo-electrocatalytic oxidation reaction (OMP removal reaction) takes place in the vicinity of the photoanode surface. The reactor is cylindrical and made up of a transparent material (i.e quartz) so that the incoming solar light can reach the photoanode. The photoanode inside the reactor has also a hollow cylindrical shape and is made up of heterojunction $BiVO_4/TiO_2$-GO to minimize the rate of recombination and enhance photo-electrocatalytic removal. Graphite is used as cathode in the reactor and a solar trough (aluminium or silver) is used to concentrate the solar light towards the reactor to achieve maximum absorbance of photons by the heterojunction photoanode. A recirculation loop after the outlet of the reactor is provided to ensure sufficient reaction time while maintaining a higher velocity to have a better mixing and minimize the partial diffusion controlled reaction [45,46]. In the recirculation loop, the outgoing water is recirculated with same initial flow rate from the inlet of the reactor, the recirculation is carried out until the removal efficiency of the photoanode for each OMP is 80 %. The CFD model was used to calculate the removal efficiency after the first circulation of

water in the reactor, the removal efficiency (percentage removal) in each recirculation was regarded the same as of the first circulation, assuming a perfect mixing in the recirculation piping and first-order reactions (removal efficiency independent of the initial concentration of OMP). Furthermore, a current density of 2.82 A m^{-2} was applied to the photoanode to enhance the kinetics of the removal reaction and to minimize the rate of recombination in the heterojunction photoanode. The value of 2.82 A m^{-2} was chosen because it corresponds to the current density at 1 V (vs Ag/AgCl) in the laboratory removal experiments.

COMOL Multiphysics software (v6.2)[1] was used to calculate the simultaneous removal of BTA, CBZ, CAF and DIC having a starting concentration of 40 μg L^{-1} in water. The following surface reaction flux equation was derived from the lab experiments (k values in Table 1) to calculate the removal of OMPs in CFD simulations [47].

$$N_{surf} = K^{*}_{surf} \times I_c \times I_L \times C \left(\text{mol. } m^{-2}.s^{-1}\right) \quad (2)$$

Where

N_{surf} = Surface reaction flux used to calculate the removal of OMPs at the surface of photoanode.

K^{*}_{surf} = experimental removal kinetic coefficient including the effect of current density and light intensity ($m^5 .A^{-1}. W^{-1}. s^{-1}$)

I_c = Current density (A m^{-2})

I_L = Solar light intensity (W m^{-2})

C = Concentration of OMPs at the surface of the photoanode (mol m^{-3})

Laminar flow and turbulent flow multiphysics packages were used in COMSOL to simulate the flow of water inside the reactor in laminar and turbulent flow conditions. Transport of dilute species (tds) package was used to calculate the removal of OMPs. At the cathode, photoanode and outer walls no slip wall conditions with default wall equations were used as boundary conditions in both laminar and turbulent flow. Similarly, normal inflow velocity with default settings was used at the inlet for both turbulent and laminar flow. Normal static pressure flow (value = 0 Pa) was used as a boundary condition for the outlet in turbulent and laminar flow conditions. For transport of dilute species (tds), at the cathode and outer walls, concentration constraint was used as a boundary condition. At the photoanode surface reaction flux given in Eq. 2 was used as condition. At the inlet, the starting concentration of the OMPs were set as boundary conditions. The important parameters used in the CFD simulations are listed in Table 1 of the supplementary information. The 2D geometrical shape shown in Fig. 1 (a) was used for 2D simulations. The length of photoanode and cathode were both 1.8 m, the height of cathode was set at 0.05 m. The 3D geometrical shape shown in Fig. 1 (b) was used for 3D simulations. The photoanode thickness was set at 0.005 m, with a total available reaction surface area (including both inner and outer surfaces) of 1.07 m^2. The overall reactor volume was 0.050 m^3, whereas the effective flow volume, excluding the solid cylindrical cathode, was 0.046 m^3. The resulting surface area to volume ratio was calculated as 23.2. Mesh element size was set as normal for both 2D and 2D simulations, the number of mesh elements for 2D configuration was around 50,000 and for 3D configuration it was around 2 million mesh elements.

Table 1
First order rate coefficients (k) of DIC, CBZ, BTA and CAF after 3 hr of treatment.

OMP	k (x 10^{-2} min^{-1})	Standard Error	R^2
Diclofenac (DIC)	3.90	1.18×10^{-4}	0,9997
Carbamazepine (CBZ)	0.430	1.41×10^{-4}	0,9697
Benzotriazole (BTA)	0.260	2.00×10^{-4}	0,9477
Caffeine (CAF)	0.240	5.10×10^{-4}	0,9571

[1] COMSOL Multiphysics v.6.2. ww.comsol.com. COMSOL AB, Stockholm, Sweden.

3. Results and discussion

3.1. Structural characterization

The crystallinity and phase composition of all the fabricated photoanodes were characterized using XRD. The XRD patterns of GO, $BiVO_4$, TiO_2-GO and $BiVO_4/TiO_2$-GO photoanodes are shown in Fig. 2. The diffraction pattern of pristine $BiVO_4$ photoanode showed fourteen broad peaks with 2θ value at 18.8°, 19.1°, 29.0°, 30.6°, 34.6°, 35.3°, 39.9°, 42.5°, 46.9°, 47.4°, 50.4°, 53.4°, 58.6° and 59.5°, which corresponds to the monoclinic scheelite phase of $BiVO_4$ (JCPDS Card No. 75–1867) [48]. The XRD pattern of the TiO_2-GO photoanode showed peaks at 25.3°, 37.7°, 48.1°, 53.9°, 55.1°and 62.7°, which are characteristic peaks of anatase TiO_2 (JCPDS Card No. 88–1175). Aditionally, the diffraction peaks at 27.4°, 36°, 41.2°and 56.6° are related to rutile TiO_2 (JCPDS Card No. 84–1286) [49]. The XRD pattern of the pure GO sample showed a minor peak at 9° (inset of Fig. 1), which is in accordance with a previous study [50]. The XRD pattern of $BiVO_4/TiO_2$-GO photoanode showed diffraction peaks of both $BiVO_4$ and TiO_2, however, the intensity of $BiVO_4$ was decreased because TiO_2-GO was deposited on top of the $BiVO_4$ photocatalytic layer. The GO diffraction peak in $BiVO_4/TiO_2$-GO photoanode could not be detected due to the lower concentration of GO in the TiO_2 matrix.

3.2. Optical properties of the fabricated photoanodes

The optical properties of the fabricated photoanodes were characterized using UV visible diffuse reflectance spectroscopy. Fig. 3 presents the absorbance spectra of $BiVO_4$, TiO_2, TiO_2-GO and $BiVO_4/TiO_2$-GO photoanodes. We observed that both the pristine $BiVO_4$ photoanode and the heterojunction $BiVO_4/TiO_2$-GO photoanode absorbed photons within the UV-visible range of the solar spectrum. In contrast, pristine TiO_2 and TiO_2-GO photoanodes showed absorption limited to the UV region, consistent with literature studies that attribute this behaviour to the intrinsic bandgap of TiO_2 and GO, which restricts photon absorption to the UV spectrum [51,52]. The combination of UV absorbing TiO_2 with $BiVO_4$ resulted in a heterojunction photoanode capable of absorbing both UV and visible light. This configuration demonstrated a lower recombination rate of photogenerated charge carriers compared to the pristine $BiVO_4$ photoanode [53]. Overall, the UV visible reflectance spectroscopy results confirmed the successful fabrication of the $BiVO_4/TiO_2$-GO heterojunction photoanode, which is driven by UV-visible light. Combining UV light absorbing TiO_2 and $BiVO_4$ layer resulted in the UV-visible absorbing heterojunction photoanode, which has lower rate of recombination of photogenerated charge carriers as compared to pristine $BiVO_4$ layer [53]. Overall, the results of UV visible reflectance spectroscopy results confirmed the successful fabrication of the $BiVO_4/TiO_2$-GO heterojunction photoanode, which is driven by UV-visible light.

3.3. Photoelectrocatalytic removal of selected OMPs

Fig. S. 2 in the supplementary information shows the removal efficiencies of the selected OMPs as a result of photolysis under simulated solar light. After 3 hr of photolysis, removal efficiency of BTA, CBZ and CAF was less than 10 % and DIC showed a removal efficiency of 60 %. The higher removal efficiency of DIC after photolysis is consistent with the literature because it absorbs photons within the UV range of the solar spectrum [38]. The low removal efficiency of BTA, CBZ and CAF is also in line with the literature because their removal reaction kinetics is very slow under simulated solar light [54,55]. Fig. 4 (a) shows the removal efficiency of pristine $BiVO_4$ and heterojunction $BiVO_4/TiO_2$-GO photoanodes for the simultaneous PEC removal of BTA, CBZ, CAF and DIC in

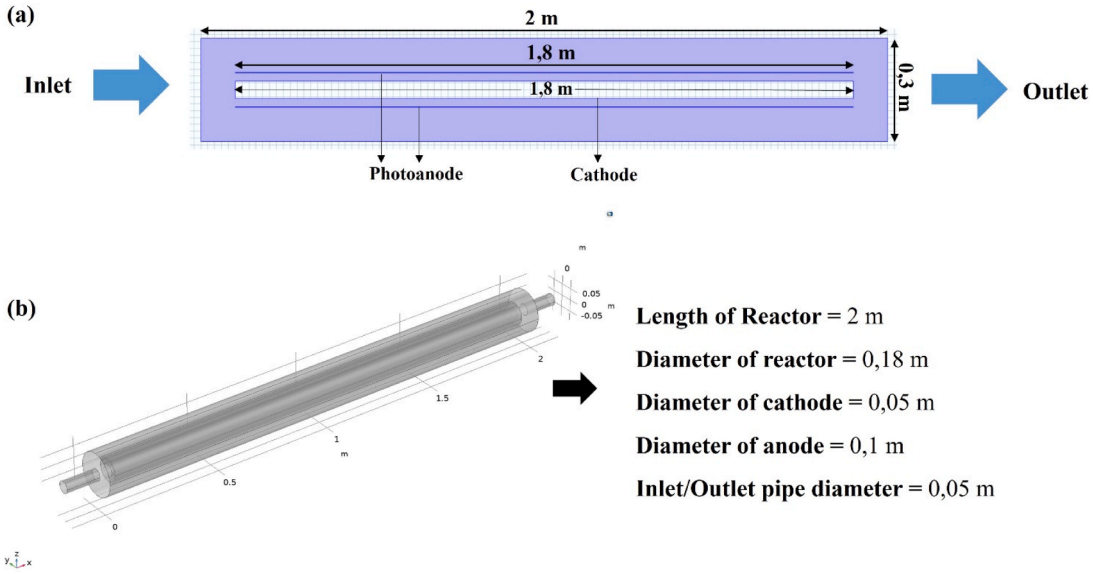

Fig. 1. Geometrical shape of the photo-electrocatalytic reactor used in 2D (a) and 3D (b) CFD simulations.

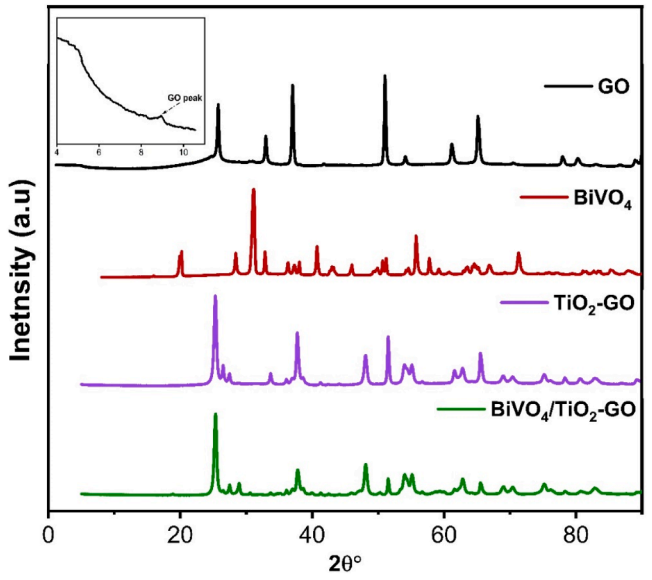

Fig. 2. XRD patterns of $BiVO_4$, GO, TiO_2-GO and $BiVO_4/TiO_2$-GO photoanodes showing characteristic diffraction peaks.

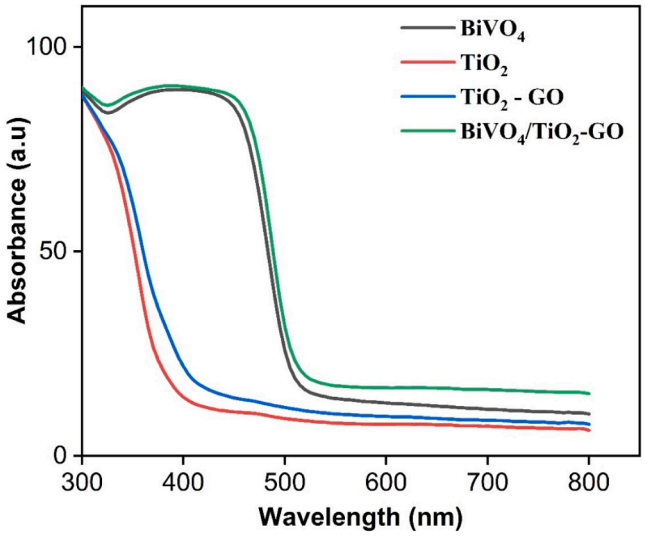

Fig. 3. UV-Visible absorbance spectrums of $BiVO_4$, TiO_2, TiO_2-Go and $BiVO_4/TiO_2$-GO photoanodes showing absorbance pattern of the fabricated photoanodes.

demineralized water. Compared to the pristine $BiVO_4$ photoanode, the $BiVO_4/TiO_2$-GO photoanode showed 50 % higher removal efficiency for BTA, CBZ and CAF. This difference in the removal efficiency was attributed to the formation of a heterojunction between the $BiVO_4$ and TiO_2-GO photocatalytic layers, which resulted in a reduction in the recombination rate of photogenerated electron-hole pairs. The coupling of photocatalytic layers of $BiVO_4$ and TiO_2-GO resulted in a built-in electric field in the $BiVO_4/TiO_2$-GO heterojunction [56]. After the irradiation of the photoanode under UV-visible light, the photogenerated electrons in the conduction band of $BiVO_4$ were transferred to the conduction band of TiO_2 under the influence of the heterojunction. At the same time, the high energy holes in the valence band of the TiO_2 were transferred to the valence band of $BiVO_4$ [57]. This improved separation of photogenerated charge carriers, reduced the recombination rate and increased the in-situ production of reactive species ($^{\bullet}OH$ and $^{\bullet}O_2^-$), which ultimately enhanced the overall removal of OMPs.

Fig. S. 3 in the supplementary information shows the average removal efficiency of the heterojunction $BiVO_4/TiO_2$-GO photoanode for all four OMPS based on triplicate experiments, along with the corresponding standard errors. Fig 4 (b) shows the fitting of the first order reaction rate equation ($C/C_0=e^{-kt}$) for the selected OMPs to determine the rate coefficient (k) for the selected OMPs. The first order rate coefficients of BTA, CBZ, CAF and DIC are shown in Table 1. The rate coefficient of DIC was higher than that of CBZ, CAF and BTA. Fig. 4 (b) also shows the normalized removal of BTA, CBZ, CAF and DIC in demineralized water by using heterojunction $BiVO_4/TiO_2$-GO photoanode at an applied voltage of 1 V (vs Ag/AgCl as the reference electrode). Fig. 3 (b) shows that the pattern of normalized removal of the selected OMPs varies, DIC showed a faster removal compared to the other OMPs. The removal kinetics of CAF and BTA were almost equal whereas the removal kinetics of CBZ was higher compared to CAF and BTA. DIC showed faster removal kinetics compared to other OMPs because of the combination of photolysis and PEC based AOP removal reaction. The difference in the normalized removal of the selected OMPs was probably due to the chemical structure of the selected OMPs. Diclofenac (DIC) has

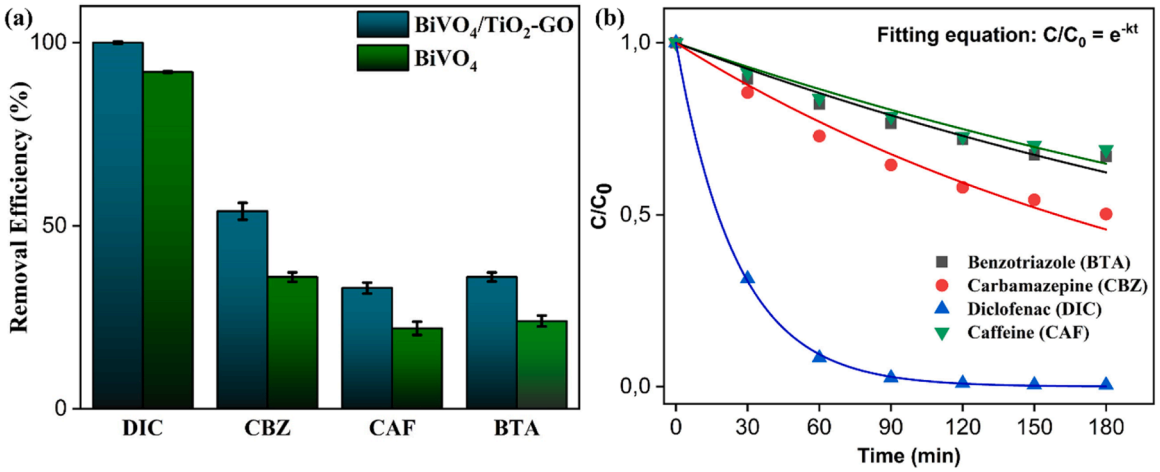

Fig. 4. (a) Comparison of removal efficiencies achieved by $BiVO_4$ and $BiVO_4/TiO_2$-GO photoanode for DIC, CBZ, CAF and BTA after 3 hr of removal experiments (b) Normalized removal profiles of DIC, CBZ, CAF and BTA using $BiVO_4/TiO_2$-GO photoanode, along with the corresponding fit to a first order reaction model.

a secondary amine group that serves as an electron donating group, making it susceptible to the attack by $^{\bullet}OH$ and $^{\bullet}O_2^-$ radicals. The oxidation reaction is likely initiated by the C-N bond cleavage due to radical ($^{\bullet}OH$ and $^{\bullet}O_2^-$) attack, resulting in the formation of 2,6-dichloroaniline as a primary intermediate [58]. Similarly, the presence of amine groups and olefinic bonds in CBZ made it more susceptible to the attack by $^{\bullet}OH$ and $^{\bullet}O_2^-$ radicals compared to CAF and BTA, which have a deficiency of electron donating functional groups. The degradation pathway of benzotriazole (BTA) is likely influenced by hydroxylation, addition, and cleavage of the phenyl ring, facilitated by •OH [59]. The process could be initiated by hydroxyl radicals (•OH) attacking the regions of high electron density within the BTA molecule, leading to the formation of hydroxylated intermediates. Subsequently, ring opening reactions can occur, resulting in the generation of aldehyde- and carboxyl- containing intermediates, ultimately leading to complete mineralization [60]. In CBZ, the olefinic double bond is most likely the primary reactive site that initiates the radical ($^{\bullet}OH$ and $^{\bullet}O_2^-$) attack on the CBZ molecule [61]. This initial reaction triggers a series of oxidative transformations, leading to the breakdown of CBZ into short-chain fatty acids or other small organic intermediates until its complete mineralization [62]. For the removal of CAF, the oxidation is most likely initiated by the •OH attack on the carbon-carbon double bond ? [63]. After a series of successive hydroxylation and oxidation reactions, dimethylparabanic acid and di (hydroxymethyl) parabanic acid can be formed as the main intermediates [64]. These intermediates can undergo further oxidation and gradually be completely mineralized. This difference in the chemical characteristics and degradation pathways of the OMPs led to the difference in reaction rate coefficient of reactive species ($^{\bullet}OH$ and $^{\bullet}O_2^-$ radicals) with the OMPs, which ultimately resulted in different removal kinetics of the OMPs during 3 hr of treatment time. Based on literature, the reaction rate coefficients (K_{OH}) of the $^{\bullet}OH$ with the selected OMPs are different for each OMP. DIC has the highest K_{OH} (8.38×10^9 L mol^{-1} s^{-1}) followed by CBZ (8.02×10^9 L mol^{-1} s^{-1}), BTA (7.6×10^9 L mol^{-1} s^{-1}) and CAF (6.40×10^9 L mol^{-1} s^{-1}) [65,66]. Moreover, there is also a possibility of direct oxidation of OMPs by the photogenerated holes generated in the heterojunction photoanode [13]. The difference in the chemical structure could also influence the direct oxidation of the selected OMPs by the photogenerated holes [19]. Similarly, the difference in the K values of the OMPs was attributed to the difference in their chemical structures, which affected their reactivity with the $^{\bullet}OH$, $^{\bullet}O_2^-$ and photo-generated holes.

The rate coefficients presented in Table 1 are comparable to, or higher than, those reported in previous studies using PEC based AOP for the removal of different pharmaceuticals such as sulfamethoxazole (10 mg L^{-1}; k = 7.40×10^{-3} min^{-1}) [67], bisphenol A (10 mg L^{-1}; k = 4.1×10^{-2} min^{-1}) [18], norfloxacin (10 mg L^{-1}; k = 6.41×10^{-3} min^{-1}) [68], tetracycline hydrochloride (20 mg L^{-1}; k = 6.42×10^{-2} min^{-1}) [69], ciprofloxacin (10 mg L^{-1}; k = 6.05×10^{-3} min^{-1}) [70] and dyes such as orange II (20 mg L^{-1}; k = 1.40×10^{-2} min^{-1}) [71] and rhodamine B (10 mg L^{-1}; k = 7.32×10^{-3} min^{-1}) [68]. Although these studies used pollutant concentrations ranging from 8 and 20 mg L^{-1}, The corresponding first order rate coefficients are not significantly higher than those in our work. Furthermore, most studies used an external bias between 1 and 2 V vs Ag/AgCl and achieved approximately 80 % removal of pollutants within an average time of about 2.5 hours. In this study PEC based simultaneous removal of BTA, CAF, CBZ and DIC showed similar removal kinetics to those reported in the literature under comparable electrical energy inputs. The results of the reusability experiments are shown in Fig. S. 4 of the supplementary information. Heterojunction photoanode showed good reusability performance as the removal efficiency was only 12 % lower for CBZ and 8 % for BTA, CAF and DIC after the three consecutive experiments. This decrease in the efficiency was most likely due to the adsorption of unoxidized intermediate product molecules within the surface cracks of the photoanode, reducing the active surface area available for the production of reactive species ($^{\bullet}OH$ and $^{\bullet}O_2^-$).

3.4. CFD simulation

The CFD simulations were first carried out in 2D geometry by constructing a geometry as shown in Fig. 4 (a). In this geometry, water entered from the inlet (left side), and the removal reaction took place at the photoanode. The distance between the anode and cathode was fixed at 5 cm, and the distance between the photoanode and the outer wall of the reactor was fixed at 10 cm. Laminar flow regime (28 L/min) and turbulent flow regime (61.6 L/min) were tested in the 2D geometry to assess the effect of flow conditions on the overall removal of the OMPs. The Reynolds number (Re) for the system was calculated using the reactor diameter as the characteristic length and the inlet velocity, with the properties of the working fluid taken into account. For the laminar flow regime, the Re was calculated as 1415, while for the turbulent flow regime, it was 3112. Further details on the Re calculations are provided in the supplementary information (Fig. S. 5, Fig. S. 6). In our CFD simulations, the selection of boundary conditions was based on both the physical principles controlling the fluid flow and established modelling practices [72]. No-slip wall conditions were applied to the cathode, photoanode and outer walls to accurately capture boundary layer formation and shear stress effects. The inlet velocity and outlet pressure conditions were specified based on experimental and design parameters to ensure realistic flow field development. These carefully chosen

conditions played a critical role in determining mass transfer rates, reaction kinetics and overall reactor performance. These boundary conditions played a major role in minimizing numerical errors and enhancing simulation reliability.

Fig. 5 (a) shows the concentration profile of DIC in turbulent flow regime after a single pass. The concentration profile in laminar flow regime indicated that the DIC concentration only decreased within the vicinity of the photoanode, removal efficiency of DIC in laminar flow regime was 11 % as shown in table next to Fig. 5 (a). The concentration profiles of other OMPs were similar in the vicinity of the photoanode, indicating that there was no removal in the bulk solution due to the short lifetime of $^{\bullet}OH$ and $^{\bullet}O_2^-$ radicals further away from the photoanode. In turbulent flow regime the removal of OMPs was enhanced as shown in table next to Fig. 5 (a) likely due to better mixing and diffusion of OMP molecules from the bulk towards the surface of the photoanode. The residence time in turbulent flow conditions was lower compared to laminar flow due to higher flow rate. In turbulent flow conditions, the removal of OMPs after two circulations are shown in the tables next to Fig. 5 (a), (b) and (c) to compare the removal in laminar flow conditions within same residence time. To increase the diffusion of OMP molecules from the bulk to the surface of the photoanode, a different design with inlet in the bottom, as shown in Fig. 5 (b), was tested in both laminar and turbulent flow regimes. Again, the turbulent flow regime showed better removal of OMPs compared to laminar flow conditions as shown in table next to Fig. 5 (b). To confirm the positive effect of mixing on the removal efficiency of OMPs, a design as shown in Fig. 5 (c) with increased obstacles was tested in both laminar and turbulent flow regimes. The design shown in Fig. 5 (c) was tested to observe the effect of additional mixing on the reactor's removal efficiency. The practical implementation of that design for the construction of the reactor would be quite challenging. The enhanced OMPs removal under turbulent flow regime is due to different factors, which include convective mass transfer, diffusion rates, hydrodynamic conditions and surface interactions [73]. Mass transfer is a critical factor in PEC based AOPs, as OMP removal is dependent on the transport of OMP molecules to the photoanode surface where the oxidation reaction occurs [12]. In laminar flow, mass transport was controlled by molecular diffusion, resulting in the formation of a thick concentration boundary layer at the photoanode-electrolyte interface. This boundary layer could have acted as a barrier to the transport of OMP molecules, thereby limiting reaction rates. The turbulent flow induced eddy diffusion and convective mixing, which reduced the thickness of the concentration boundary layer. The ratio of convective to diffusive mass transfer increases under turbulent conditions, which results in a higher mass transfer coefficient [74]. As a result, the OMP removal was enhanced due to the increased mass transfer of OMPs reaching the photoanode surface. Moreover, the diffusion of reactive species ($^{\bullet}OH$ and $^{\bullet}O_2^-$) is also enhanced under turbulent flow condition [72]. Turbulent flow could also prevent the excessive accumulation of reaction intermediates at the photoanode surface, thereby maintaining the high catalytic activity of the photocatalysts. Fig. 5 (d) shows a more practical design for the construction of the reactor, and it was tested to investigate the effect of decreasing the distance between the outer wall of the reactor and the photoanode (referred to as depth) of the reactor on the residence time and removal of OMPs under turbulent

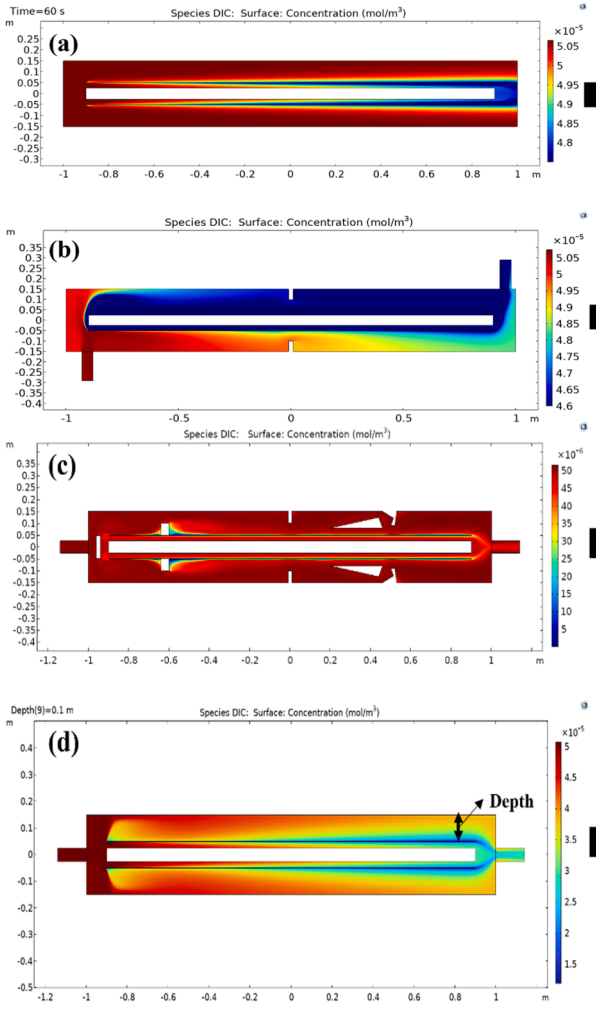

Flow Condition	Residence Time (min)	CAF Removal (%)	BTA Removal (%)	CBZ Removal (%)	DIC Removal (%)
Laminar	4.2	2.5	2.5	4.2	11
Turbulent	4 (2 circulations)	5.1	5.2	9.6	20

Flow Condition	Residence Time (min)	CAF Removal (%)	BTA Removal (%)	CBZ Removal (%)	DIC Removal (%)
Laminar	4.2	3.5	3.6	6.7	12
Turbulent	4 (2 circulations)	7.2	7.2	11.6	24

Flow Condition	Residence Time (min)	CAF Removal (%)	BTA Removal (%)	CBZ Removal (%)	DIC Removal (%)
Laminar	4.2	4.2	4.2	7.8	16
Turbulent	4 (2 circulations)	8.3	8.3	14.6	30

Flow Condition	Residence Time (min)	CAF Removal (%)	BTA Removal (%)	CBZ Removal (%)	DIC Removal (%)
Turbulent	2	5.0	5.4	8.5	30

Fig. 5. Different designs tested using CFD in 2D geometry along with the removal performance (tables on right) in turbulent and laminar flow conditions.

flow regime. Table 2 shows the effect of changing the depth of the reactor on the removal of OMPs. By decreasing the depth of the reactor the velocity increased and residence time (treatment time) decreased, without affecting the removal of OMPs after a single treatment pass. The removal remained unchanged because the shorter residence time is compensated by a decreasing bulk zone (without reaction), allowing more surface reaction at the photoanode. The number of recirculations to achieve 80 % removal was not reduced by decreasing the depth of the reactor. However, the total treatment time for 80 % removal was reduced by 60 % when the depth was changed from 0.10 m to 0.02 m, because the velocity increases when the depth decreases. Achieving a depth of 0.02 m would be quite challenging during the construction of the reactor. Nevertheless, a depth in the range of 0.05 – 0.06 m would be more practical for the construction of the reactor.

For the 3D simulation, the design shown in Fig. 1 (b) was used and it was based upon the design in 2D shown in Fig. 5 (d). Turbulent flow regime (61.6 L/min) was used to simulate photo-electrocatalytic removal of OMPs. The simulated results are depicted in Fig. 6 (a) as a cross-sectional view through the central axis of the cylindrical reactor, displaying the concentration profile of DIC along its length. It was observed in Fig. 6 (a) that the concentrations of OMPs are higher at the inner side of the photoanode. This limited removal of OMPs at the inner side of photoanode was attributed to the high flow velocity at the inner side compared to the outer side of photoanode, as shown in the velocity profile (Fig. 6 (b)). To achieve a more uniform velocity profile in the reactor, the inlet pipe diameter was increased and set equal to the diameter of the reactor. Fig. 6 (c) shows the concentration profile of DIC with the inlet pipe diameter equal to the diameter of the reactor. Increasing the diameter of the inlet pipe had a negative impact on the removal efficiency of the reactor because the flow velocity (Fig. 6 (d)) was higher at the outer side of the photoanode, leading to lower removal of OMPs at the outer side of the photoanode compared to the inner side. The removal of all OMPs was lower and the number of recirculations for 80 % removal along with the total treatment time also increased compared to the first configuration (Fig. 6 (a)), as shown in Table 3. In the next step, the diameter of the photoanode was increased to 0.14 m to allow for a more uniform distribution of flow and to increase the surface area of the photoanode. The diameter of the inlet pipe was set equal to the diameter of the reactor. Fig. 6 (e) shows the sliced concentration profile of DIC with increased diameter of photoanode. This had a positive impact on the removal performance (Table 3) of the reactor as the total treatment time was reduced by 43 %, compared to the previous two configurations (Fig. 6 (a) and Fig. 6 (c)). Moreover, the flow velocity (Fig. 6 (f)) was more uniform inside the reactor compared to first (Fig. 6 (a)) and second configuration (Fig. 6 (c)). Therefore, the results of the third configuration were regarded as more efficient and applicable for pilot testing and experimental validation. The effect of light intensity on the optimized configuration was also tested in 3D simulation. Table 2 in the supplementary information highlights the impact of light intensity on the removal efficiency of the PEC reactor. A notable reduction in the removal of OMPs was observed when the light intensity was lowered from 400 W m^{-2} to 100 W m^{-2}. At lower intensity, the production yield of $^{\bullet}OH$ and $^{\bullet}O_2^-$ is decreased, therefore, the removal kinetics also slows down which decreases the removal [19]. With lower light intensity of 100 W m^{-2}, the total time for 80 % removal of OMPs was also more than three times higher compared to 400 W m^{-2}. This effect of light intensity on the removal efficiency of the reactor could be regarded as a limitation of the PEC based AOP removal.

In our study, the CFD simulations primarily considered fluid flow conditions, reactor depth and light intensity as the main variables in the model. Incorporating additional variables such as electrode arrangement, light intensity distribution, and chemical reaction kinetics into the model would provide deeper insights into reactor optimization. These factors could be crucial for maximizing removal efficiency and scalability. However, their inclusion would require the development of coupled multi-physics models, which is beyond the scope of the current study. For the CFD simulations, our primary objective was to simulate the photo-electrochemical environment and hydrodynamic conditions. We suggest that future work should address these additional variables to enhance model robustness and further optimize reactor design.

Several challenges must be addressed to translate CFD simulations into practical larger scale applications. The prolonged use of the heterojunction photoanode can lead to material degradation, particularly during the time of high intensity solar irradiation and high flow rate. Strategies such as the development of (porous) protective coatings are crucial to enhance the long-term stability of the photoanode. Similarly, the photoanode in the PEC reactor would be susceptible to fouling (including biofilm growth) and organic matter deposition. The effective use of hydrodynamic shear forces, periodic electrode cleaning and antifouling coatings is necessary to address these issues. The energy consumption of large scale PEC reactors is a critical factor in assessing their environmental impact and sustainability. Renewable energy integration and process optimization can minimize environmental impacts. Moreover, the stability of photoanodes in large scale reactors under long term operation must be evaluated to prevent secondary pollution from photocatalyst degradation.

4. Conclusions

In this investigation, a heterojunction $BiVO_4/TiO_2$-GO photoanode was successfully fabricated using an ultrasonic spray pyrolysis (USP) process. Characterization via XRD and UV-visible diffusive reflectance spectroscopy confirmed the formation of UV-visible light absorbing heterojunction photoanodes. The heterojunction photoanode at an applied voltage of 1 V (vs Ag/AgCl) achieved simultaneous removal efficiencies of 100 % for DIC, 54 % for CBZ, 36 % for BTA and 33 % for BTA under simulated solar light. The heterojunction photoanode demonstrated a 50 % increase in the removal efficiency for BTA, CBZ, and CAF compared to the pristine $BiVO_4$ photoanode. This increase in the removal efficiency was attributed to the improved charge separation in the heterojunction photoanode.

CFD simulations provided further insight into the reactor performance by elucidating the effects of flow dynamics on mass transport phenomena. Specifically, the simulations revealed that a turbulent flow

Tabel 2
Effect of depth of reactor (as shown in Fig. 3 (d)) on the residence time and removal performance of the reactor towards 80 % removal of DIC, CBZ, CAF and BTA.

Depth (m)	Residence Time (min)	CAF Removal (%)	BTA Removal (%)	CBZ Removal (%)	DIC Removal (%)	No. Of Circulations For 80% Removal	Total Time For 80% Removal
0.1	1.94	5.0	5.4	8.6	30	32	61 min
0.09	1.78	5.0	5.4	8.6	30	32	57 min
0.08	1.63	5.0	5.4	8.6	30	32	52 min
0.07	1.48	5.0	5.4	8.6	30	32	47 min
0.06	1.33	5.0	5.4	8.6	30	32	42 min
0.05	1.17	5.0	5.4	8.6	30	32	37 min
0.04	1.02	5.0	5.4	8.6	30	32	33 min
0.03	0.87	5.0	5.4	8.6	30	32	28 min
0.02	0.71	5.0	5.4	8.6	30	32	23 min

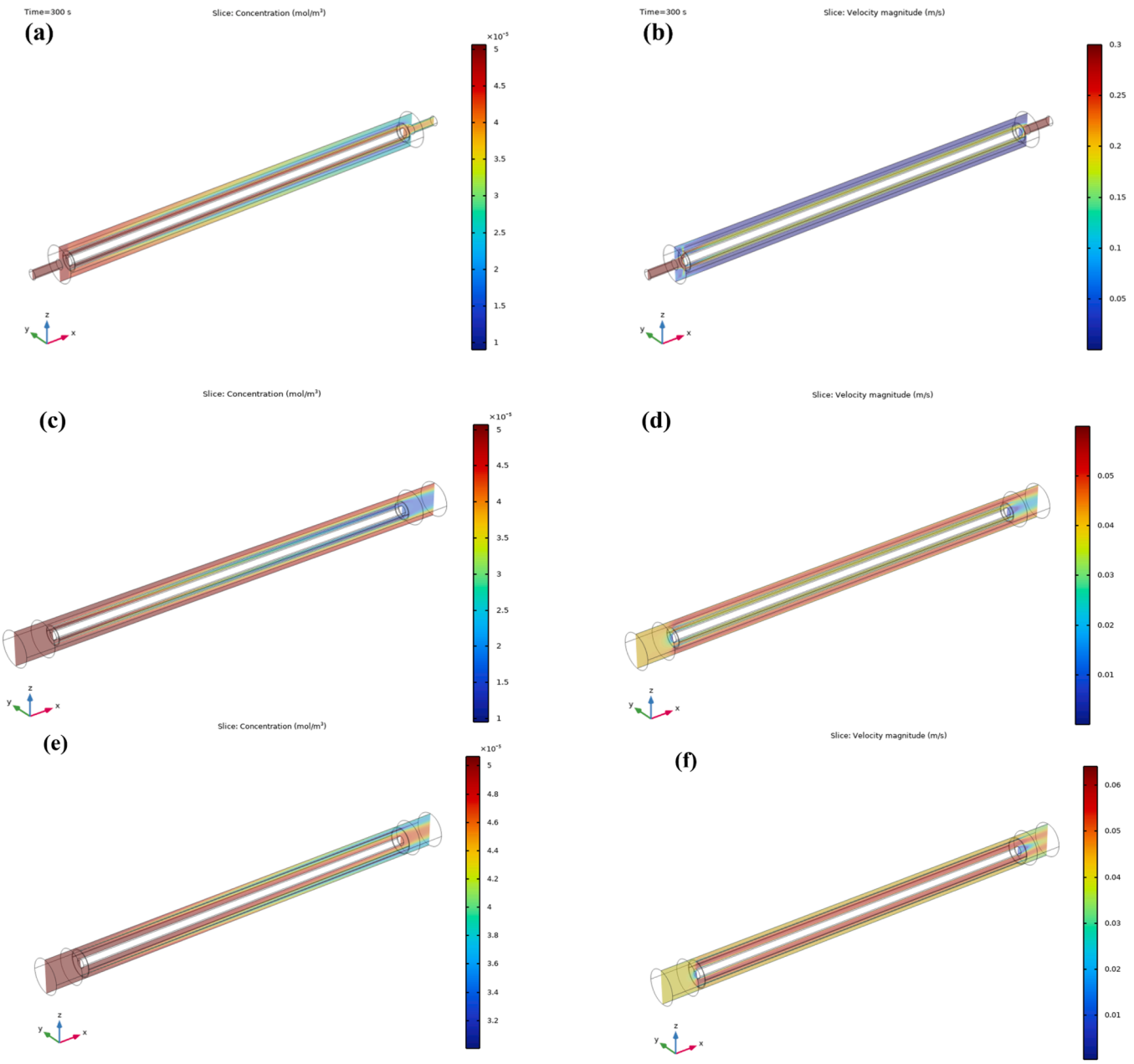

Fig. 6. 3D CFD simulations of photoelectrocatalytic reactor, showing the effect of inlet pipe diameter (a,b,c,d) and photoanode diameter (e,f) on the concentration profile and velocity magnitude profile of DIC.

Tabel 3
Removal performance in 3D CFD simulations, showing the effect of photoanode diameter and inlet pipe diameter.

Inlet pipe diameter (m)	Photoanode diameter (m)	Residence time (s)	CAF Removal (%)	BTA Removal (%)	CBZ Removal (%)	DIC Removal (%)	No. Of Circulations For 80% Removal	Total Time For 80% Removal
0.05	0.1	43	4	4	6	33	40	29 min
0.18	0.1	43	3	4	6	28	53	40 min
0.18	0.14	43	5	5	8	41	32	23 min

regime substantially enhanced the diffusion of OMP molecules from the bulk solution to the photoanode surface, compared to a laminar flow regime. Under a uniform flow velocity profile and at a light intensity of 400 W m^{-2}, the optimized configuration achieved simultaneous removal efficiencies of 80 % for BTA, CBZ, CAF, and DIC within 25 mins. This result highlighted the critical influence of flow-induced mass transfer on the kinetics of OMP degradation. The CFD analysis also indicated that increasing flow velocity positively impacted the removal kinetics, offering a promising approach for scaling up the PEC reactor from laboratory to pilot scale. The integration of CFD with experimental results facilitated the optimization of reactor design. This optimization is expected to yield considerable reductions in operational time and cost during practical implementation. A key limitation of this study is the absence of uncertainty analysis of the CFD simulations. The primary

objective was to establish a fundamental understanding of fluid flow effects on OMP removal and validate the model against experimental data. We acknowledge that CFD simulations involve uncertainties due to model assumptions, numerical discretization, boundary conditions and parameter estimations. Conducting a comprehensive uncertainty analysis requires additional computational resources and extensive sensitivity studies, which were beyond the scope of our study. Future research will integrate uncertainty quantification techniques such as global sensitivity analysis to improve the predictive reliability and robustness of CFD based reactor design under varying conditions. Additionally, long term investigation into the stability and durability of the photoanode under prolonged operational conditions is essential to assess the viability of PEC reactors in large scale applications. Future work will address these limitations, thereby advancing the development of robust PEC based AOPs for efficient and sustainable wastewater treatment.

CRediT authorship contribution statement

Agha Zeeshan Ali: Writing – review & editing, Writing – original draft, Validation, Project administration, Methodology, Investigation, Formal analysis, Conceptualization. **Yuhao Wu:** Investigation, Data curation. **Bas Wols:** Writing – review & editing, Validation, Supervision, Software, Methodology. **Mohamad Zeidan:** Writing – review & editing, Supervision, Software, Methodology, Data curation. **Henri Spanjers:** Writing – review & editing, Supervision, Project administration, Funding acquisition. **Jan Peter van der Hoek:** Writing – review & editing, Supervision, Project administration, Funding acquisition.

Declaration of competing interest

The authors declare that they have no known competing financial interests or personal relationships that could have appeared to influence the work reported in this paper.

Acknowledgements

This research was supported with a grant from the Topsector Water & Maritime TKI Water Technology Program (grant 2023TUD001) of the Ministry of Economic Affairs and Climate Change, and supported by water utility Waternet (Amsterdam, the Netherlands) and Nijhuis Saur Industries.

Supplementary materials

Supplementary material associated with this article can be found, in the online version, at doi:10.1016/j.ceja.2025.100721.

Data availability

Data will be made available on request.

References

[1] N.A. Abbasi, S.U. Shahid, M. Majid, A. Tahir, Chapter 1 - introduction to environmental micropollutants, in: M.Z. Hashmi, S. Wang, Z. Ahmed (Eds.), Environmental Micropollutants, Elsevier, 2022, pp. 1–12, https://doi.org/10.1016/B978-0-323-90555-8.00010-6.

[2] Y. Luo, W. Guo, H.H. Ngo, L.D. Nghiem, F.I. Hai, J. Zhang, S. Liang, X.C. Wang, A review on the occurrence of micropollutants in the aquatic environment and their fate and removal during wastewater treatment, Sci. Total Environ. 473–474 (2014) 619–641, https://doi.org/10.1016/j.scitotenv.2013.12.065.

[3] D. Bunke, S. Moritz, W. Brack, D.L. Herráez, L. Posthuma, M. Nuss, Developments in society and implications for emerging pollutants in the aquatic environment, Environ. Sci. Eur. 31 (2019) 32, https://doi.org/10.1186/s12302-019-0213-1.

[4] A.T. Besha, A.Y. Gebreyohannes, R.A. Tufa, D.N. Bekele, E. Curcio, L. Giorno, Removal of emerging micropollutants by activated sludge process and membrane bioreactors and the effects of micropollutants on membrane fouling: a review, J. Environ. Chem. Eng. 5 (2017) 2395–2414, https://doi.org/10.1016/j.jece.2017.04.027.

[5] M.A. Abbas, M. Iqbal, H.M. Tauqeer, V. Turan, M. Farhad, Chapter 16 - microcontaminants in wastewater, in: M.Z. Hashmi, S. Wang, Z. Ahmed (Eds.), Environmental Micropollutants, Elsevier, 2022, pp. 315–329, https://doi.org/10.1016/B978-0-323-90555-8.00018-0.

[6] V. Vinayagam, K.N. Palani, S. Ganesh, S. Rajesh, V.V. Akula, R. Avoodaiappan, O. S. Kushwaha, A. Pugazhendhi, Recent developments on advanced oxidation processes for degradation of pollutants from wastewater with focus on antibiotics and organic dyes, Environ. Res. 240 (2024) 117500, https://doi.org/10.1016/j.envres.2023.117500.

[7] Z.A. Yacouba, J. Mendret, G. Lesage, F. Zaviska, S. Brosillon, Removal of organic micropollutants from domestic wastewater: the effect of ozone-based advanced oxidation process on nanofiltration, J. Water. Process. Eng. 39 (2021) 101869, https://doi.org/10.1016/j.jwpe.2020.101869.

[8] P. Koundle, N. Nirmalkar, M. Momotko, S. Makowiec, G. Boczkaj, Tetracycline degradation for wastewater treatment based on ozone nanobubbles advanced oxidation processes (AOPs) – Focus on nanobubbles formation, degradation kinetics, mechanism and effects of water composition, Chem. Eng. J. 501 (2024) 156236, https://doi.org/10.1016/j.cej.2024.156236.

[9] Y. Yan, B. Lin, L. Zhang, Y. Wang, H. Zhang, H. Zheng, T. Zhou, Y. Zhan, Z. Yu, Y. Kuang, J. Tang, Electrochemical oxidation processes based on renewable energy towards carbon neutrality: oxidation fundamentals, catalysts, challenges and prospects, Chem. Eng. J. 487 (2024) 150447, https://doi.org/10.1016/j.cej.2024.150447.

[10] T. Zhou, J. Du, Z. Wang, G. Xiao, L. Luo, M. Faheem, H. Ling, J. Bao, Degradation of sulfamethoxazole by MnO2/heat-activated persulfate: kinetics, synergistic effect and reaction mechanism, Chem. Eng. J. Adv. 9 (2022) 100200, https://doi.org/10.1016/j.ceja.2021.100200.

[11] J.E. Kumar, T. Mulai, W. Kharmawphlang, R.N. Sharan, M.K. Sahoo, The efficiency of Fenton, Fenton/MW and UV/oxidant processes in the treatment of a mixture of higher concentrations of azo dyes, Chem. Eng. J. Adv. 15 (2023) 100515, https://doi.org/10.1016/j.ceja.2023.100515.

[12] Q. Zhang, D. Zheng, B. Bai, Z. Ma, S. Zong, Insight into antibiotic removal by advanced oxidation processes (AOPs): performance, mechanism, degradation pathways, and ecotoxicity assessment, Chem. Eng. J. 500 (2024) 157134, https://doi.org/10.1016/j.cej.2024.157134.

[13] S. Garcia-Segura, E. Brillas, Applied photoelectrocatalysis on the degradation of organic pollutants in wastewaters, J. Photochem. Photobiol. C: Photochem. Rev. 31 (2017) 1–35, https://doi.org/10.1016/j.jphotochemrev.2017.01.005.

[14] B.O. Orimolade, B.A. Koiki, G.M. Peleyeju, O.A. Arotiba, Visible light driven photoelectrocatalysis on a FTO/BiVO4/BiOI anode for water treatment involving emerging pharmaceutical pollutants, Electrochim. Acta 307 (2019) 285–292, https://doi.org/10.1016/j.electacta.2019.03.217.

[15] M.C. Collivignarelli, A. Abbà, M.C. Miino, G. Bertanza, S. Sorlini, S. Damiani, H. Arab, M. Bestetti, S. Franz, Photoelectrocatalysis on TiO2 meshes: different applications in the integrated urban water management, Environ. Sci. Pollut. Res. 28 (2021) 59452–59461, https://doi.org/10.1007/s11356-021-12606-5.

[16] M. Liao, L. Su, Y. Deng, S. Xiong, R. Tang, Z. Wu, C. Ding, L. Yang, D. Gong, Strategies to improve WO3-based photocatalysts for wastewater treatment: a review, J. Mater. Sci. 56 (2021) 14416–14447, https://doi.org/10.1007/s10853-021-06202-8.

[17] S. Rajeswari, R. Venckatesh, Chapter 24 - ZnO-based nanoparticles for wastewater treatment: A review, in: K.A. Abd-Elsalam (Ed.), Zinc-Based Nanostructures for Environmental and Agricultural Applications, Elsevier, 2021, pp. 485–507, https://doi.org/10.1016/B978-0-12-822836-4.00022-7.

[18] H. Shao, Y. Wang, H. Zeng, J. Zhang, Y. Wang, M. Sillanpää, X. Zhao, Enhanced photoelectrocatalytic degradation of bisphenol a by BiVO4 photoanode coupling with peroxymonosulfate, J. Hazard. Mater. 394 (2020) 121105, https://doi.org/10.1016/j.jhazmat.2019.121105.

[19] B.O. Orimolade, O.A. Arotiba, Bismuth vanadate in photoelectrocatalytic water treatment systems for the degradation of organics: a review on recent trends, J. Electroanal. Chem. 878 (2020) 114724, https://doi.org/10.1016/j.jelechem.2020.114724.

[20] R. Suresh, S. Rajendran, P.S. Kumar, T.K.A. Hoang, M. Soto-Moscoso, Halides and oxyhalides-based photocatalysts for abatement of organic water contaminants – An overview, Environ. Res. 212 (2022) 113149, https://doi.org/10.1016/j.envres.2022.113149.

[21] H. Jiang, H. Dai, X. Meng, L. Zhang, J. Deng, K. Ji, Morphology-dependent photocatalytic performance of monoclinic BiVO4 for methyl orange degradation under visible-light irradiation, Chin. J. Catal. 32 (2011) 939–949, https://doi.org/10.1016/S1872-2067(10)60215-X.

[22] T. Ahmed, M. Ammar, A. Saleem, H. Zhang, H. Xu, Z-scheme 2D-m-BiVO4 networks decorated by a g-CN nanosheet heterostructured photocatalyst with an excellent response to visible light, RSC. Adv. 10 (2020) 3192–3202, https://doi.org/10.1039/C9RA09473C.

[23] O.J. Ajala, J.O. Tijani, M.T. Bankole, A.S. Abdulkareem, A critical review on graphene oxide nanostructured material: properties, synthesis, characterization and application in water and wastewater treatment, Environ. Nanotechnol. Monit. Manag. 18 (2022) 100673, https://doi.org/10.1016/j.enmm.2022.100673.

[24] E.D.H. Kong, J.H.F. Chau, C.W. Lai, C.S. Khe, G. Sharma, A. Kumar, S. Siengchin, M.R. Sanjay, GO/TiO2-related nanocomposites as photocatalysts for pollutant removal in wastewater treatment, Nanomater. 12 (2022) 3536, https://doi.org/10.3390/nano12193536.

[25] R. Loos, B.M. Gawlik, G. Locoro, E. Rimaviciute, S. Contini, G. Bidoglio, EU-wide survey of polar organic persistent pollutants in European river waters, Environ. Pollut. 157 (2009) 561–568, https://doi.org/10.1016/j.envpol.2008.09.020.
[26] H. Janna, M.D. Scrimshaw, R.J. Williams, J. Churchley, J.P. Sumpter, From dishwasher to tap? Xenobiotic substances benzotriazole and tolyltriazole in the environment, Environ. Sci. Technol. 45 (2011) 3858–3864, https://doi.org/10.1021/es103267g.
[27] E. Borowska, E. Felis, J. Kalka, Oxidation of benzotriazole and benzothiazole in photochemical processes: kinetics and formation of transformation products, Chem. Eng. J. 304 (2016) 852–863, https://doi.org/10.1016/j.cej.2016.06.123.
[28] J. Xu, L. Li, C. Guo, Y. Zhang, S. Wang, Removal of benzotriazole from solution by BiOBr photocatalysis under simulated solar irradiation, Chem. Eng. J. 221 (2013) 230–237, https://doi.org/10.1016/j.cej.2013.01.081.
[29] Â. Almeida, A.M.V.M. Soares, V.I. Esteves, R. Freitas, Occurrence of the antiepileptic carbamazepine in water and bivalves from marine environments: a review, Environ. Toxicol. Pharmacol. 86 (2021) 103661, https://doi.org/10.1016/j.etap.2021.103661.
[30] D.P. Mohapatra, S.K. Brar, R.D. Tyagi, P. Picard, R.Y. Surampalli, Analysis and advanced oxidation treatment of a persistent pharmaceutical compound in wastewater and wastewater sludge-carbamazepine, Sci. Total Environ. 470–471 (2014) 58–75, https://doi.org/10.1016/j.scitotenv.2013.09.034.
[31] N.A. Mansor, K.S. Tay, Potential toxic effects of chlorination and UV/chlorination in the treatment of hydrochlorothiazide in the water, Sci. Total Environ. 714 (2020) 136745, https://doi.org/10.1016/j.scitotenv.2020.136745.
[32] C. Liu, Z.T. How, Y. Ju, L. Feng, X. Ren, M. Gamal El-Din, Experimental and theoretical insight into carbamazepine degradation by chlorine-based advanced oxidation processes: efficiency, energy consumption, mechanism and DBPs formation, J. Environ. Sci. 139 (2024) 72–83, https://doi.org/10.1016/j.jes.2023.05.012.
[33] R. Shaddel, S. Rajabi-Moghaddam, Encapsulation of caffeine in chitosan-coated nanoliposomes and its application in drink formulation, Food Hydrocoll. 149 (2024) 109598, https://doi.org/10.1016/j.foodhyd.2023.109598.
[34] M.T. Pham, T.T.H. Chu, D.C. Vu, Mitigation of caffeine micropollutants in wastewater through Ag-doped ZnO photocatalyst: mechanism and environmental impacts, Environ. Geochem. Health 46 (2024) 168, https://doi.org/10.1007/s10653-024-01952-1.
[35] M.R. Karim, A. Mohammad, C.B. Mukta, J. Lee, T. Yoon, Biofilm-engineered fabrication of Ag nanoparticles with modified ZIF-8-derived ZnO for a high-performance supercapacitor, J. Energy. Storage. 75 (2024) 109646, https://doi.org/10.1016/j.est.2023.109646.
[36] P. Sathishkumar, R.A.A. Meena, T. Palanisami, V. Ashokkumar, T. Palvannan, F. L. Gu, Occurrence, interactive effects and ecological risk of diclofenac in environmental compartments and biota - a review, Sci. Total Environ. 698 (2020) 134057, https://doi.org/10.1016/j.scitotenv.2019.134057.
[37] Z. Wang, S. Guo, B. Zhang, J. Fang, L. Zhu, Interfacially crosslinked β-cyclodextrin polymer composite porous membranes for fast removal of organic micropollutants from water by flow-through adsorption, J. Hazard. Mater. 384 (2020) 121187, https://doi.org/10.1016/j.jhazmat.2019.121187.
[38] K. Fischer, S. Sydow, J. Griebel, S. Naumov, C. Elsner, I. Thomas, A.A. Latif, A. Schulze, Enhanced removal and toxicity decline of Diclofenac by combining UVA treatment and adsorption of photoproducts to polyvinylidene difluoride, Polymers (Basel) 12 (2020) 2340, https://doi.org/10.3390/polym12102340.
[39] Verwijdering van organische microverontreinigingen. Handvatten voor de keuze van behandelingstechniek in combinatie met de benodigde hydraulische capaciteit | STOWA, (2020). https://www.stowa.nl/publicaties/verwijdering-van-organische-microverontreinigingen-handvatten-voor-de-keuze-van (accessed February 7, 2025).
[40] S.E. Jujjavarapu, T. Kumar, S. Gupta, CFD modelling for optimization of wastewater treatment processes: Towards a low-cost cleaner future tool, in: S. E. Jujjavarapu, T. Kumar, S. Gupta (Eds.), Computational Fluid Dynamics Applications in Bio and Biomedical Processes: Biotechnology Applications, Springer Nature, Singapore, 2024, pp. 35–70, https://doi.org/10.1007/978-981-99-7129-9_2.
[41] B. Devipriya, S. Mohanan, A. Surenjan, CFD modelling of an immobilised photocatalytic reactor for phenol degradation, Water Sci. Technol. 88 (2023) 2121–2135, https://doi.org/10.2166/wst.2023.306.
[42] R.P.M. Moreira, G.L. Puma, Multiphysics computational fluid-dynamics (CFD) modeling of annular photocatalytic reactors by the discrete ordinates method (DOM) and the six-flux model (SFM) and evaluation of the contaminant intrinsic kinetics constants, Catal. Today 361 (2021) 77–84, https://doi.org/10.1016/j.cattod.2020.01.012.
[43] H. Seyyedbagheri, R. Alizadeh, B. Mirzayi, M. Valibeknejad, Modeling and CFD simulation of photocatalytic removal of tetracycline by ZnO/PbBiO2Cl nanocomposite catalyst, J. Mol. Liq. 399 (2024) 124398, https://doi.org/10.1016/j.molliq.2024.124398.
[44] A.Z. Ali, Y. Wu, Y.-D. Bennani, H. Spanjers, J.P. van der Hoek, Photo-electrocatalytic based removal of acetaminophen: application of visible light driven heterojunction based BiVO4/BiOI photoanode, Chemosphere 324 (2023) 138322, https://doi.org/10.1016/j.chemosphere.2023.138322.
[45] G. Sagawe, R.J. Brandi, D. Bahnemann, A.E. Cassano, Photocatalytic reactors for treating water pollution with solar illumination: A simplified analysis for *n*-steps flow reactors with recirculation, Sol. Energy 79 (2005) 262–269, https://doi.org/10.1016/j.solener.2004.11.010.
[46] A. Sraw, T. Kaur, Y. Pandey, A. Sobti, R.K. Wanchoo, A.P. Toor, Fixed bed recirculation type photocatalytic reactor with TiO2 immobilized clay beads for the degradation of pesticide polluted water, J. Environ. Chem. Eng. 6 (2018) 7035–7043, https://doi.org/10.1016/j.jece.2018.10.062.
[47] L. Suhadolnik, A. Pohar, U. Novak, B. Likozar, A. Mihelič, M. Čeh, Continuous photocatalytic, electrocatalytic and photo-electrocatalytic degradation of a reactive textile dye for wastewater-treatment processes: batch, microreactor and scaled-up operation, J. Ind. Eng. Chem. 72 (2019) 178–188, https://doi.org/10.1016/j.jiec.2018.12.017.
[48] K. Zhang, Y. Liu, J. Deng, S. Xie, X. Zhao, J. Yang, Z. Han, H. Dai, Co–Pd/BiVO4: high-performance photocatalysts for the degradation of phenol under visible light irradiation, Appl. Catal. B: Environ. 224 (2018) 350–359, https://doi.org/10.1016/j.apcatb.2017.10.044.
[49] E. Han, K. Vijayarangamuthu, J. Youn, Y.-K. Park, S.-C. Jung, K.-J. Jeon, Degussa P25 TiO2 modified with H2O2 under microwave treatment to enhance photocatalytic properties, Catal. Today 303 (2018) 305–312, https://doi.org/10.1016/j.cattod.2017.08.057.
[50] A.R. Nanakkal, L.K. Alexander, Graphene/BiVO4/TiO2 nanocomposite: tuning band gap energies for superior photocatalytic activity under visible light, J. Mater. Sci. 52 (2017) 7997–8006, https://doi.org/10.1007/s10853-017-1002-0.
[51] P. Gangwar, S. Singh, N. Khare, Study of optical properties of graphene oxide and its derivatives using spectroscopic ellipsometry, Appl. Phys. A 124 (2018) 620, https://doi.org/10.1007/s00339-018-1999-1.
[52] K.R. Reyes-Gil, D.B. Robinson, WO3-Enhanced TiO2 nanotube photoanodes for solar water splitting with simultaneous wastewater treatment, ACS. Appl. Mater. Interfaces. 5 (2013) 12400–12410, https://doi.org/10.1021/am403369p.
[53] J. Resasco, H. Zhang, N. Kornienko, N. Becknell, H. Lee, J. Guo, A.L. Briseno, P. Yang, TiO2/BiVO4 Nanowire heterostructure photoanodes based on type II band alignment, ACS. Cent. Sci. 2 (2016) 80–88, https://doi.org/10.1021/acscentsci.5b00402.
[54] H. Liu, Y. Meng, J. Li, X. Wang, T. Zhang, Mechanistic insights into UV photolysis of carbamazepine and caffeine: active species, reaction sites, and toxicity evolution, Chemosphere 308 (2022) 136418, https://doi.org/10.1016/j.chemosphere.2022.136418.
[55] C. Weidauer, C. Davis, J. Raeke, B. Seiwert, T. Reemtsma, Sunlight photolysis of benzotriazoles – Identification of transformation products and pathways, Chemosphere 154 (2016) 416–424, https://doi.org/10.1016/j.chemosphere.2016.03.090.
[56] Y. Jia, Z. Wang, Y. Ma, J. Liu, W. Shi, Y. Lin, X. Hu, K. Zhang, Boosting interfacial charge migration of TiO2/BiVO4 photoanode by W doping for photoelectrochemical water splitting, Electrochim. Acta 300 (2019) 138–144, https://doi.org/10.1016/j.electacta.2019.01.106.
[57] L. Fu, W. Lian, Y. Lin, W. Fang, R. Xv, X. Shang, Enhanced charge separation and transfer by BiVO4 heterojunction and N-doped for TiO2 nanotubes during photoelectrochemical water splitting, ACS. Appl. Energy Mater. 6 (2023) 10116–10127, https://doi.org/10.1021/acsaem.3c01747.
[58] P. Iovino, M. Lavorgna, E. Orlo, C. Russo, B. De Felice, N. Campolattano, L. Muscariello, A. Fenti, S. Chianese, M. Isidori, D. Musmarra, An integrated approach for the assessment of the electrochemical oxidation of diclofenac: by-product identification, microbiological and eco-genotoxicological evaluation, Sci. Total Environ. 909 (2024) 168511, https://doi.org/10.1016/j.scitotenv.2023.168511.
[59] S. Wang, S. Pei, J. Zhang, J. Huang, S. You, Flow-through electrochemical removal of benzotriazole by electroactive ceramic membrane, Water. Res. 218 (2022) 118454, https://doi.org/10.1016/j.watres.2022.118454.
[60] Y. Yao, Y. Xie, B. Zhao, L. Zhou, Y. Shi, Y. Wang, Y. Sheng, H. Zhao, J. Sun, H. Cao, N-dependent ozonation efficiency over nitrogen-containing heterocyclic contaminants: a combined density functional theory study on reaction kinetics and degradation pathways, Chem. Eng. J. 382 (2020) 122708, https://doi.org/10.1016/j.cej.2019.122708.
[61] C. Zhao, Z. Liao, W. Liu, F. Liu, J. Ye, J. Liang, Y. Li, Carbon quantum dots modified tubular g-C3N4 with enhanced photocatalytic activity for carbamazepine elimination: mechanisms, degradation pathway and DFT calculation, J. Hazard. Mater. 381 (2020) 120957, https://doi.org/10.1016/j.jhazmat.2019.120957.
[62] Y. Li, Y. Yang, J. Lei, W. Liu, M. Tong, J. Liang, The degradation pathways of carbamazepine in advanced oxidation process: a mini review coupled with DFT calculation, Sci. Total Environ. 779 (2021) 146498, https://doi.org/10.1016/j.scitotenv.2021.146498.
[63] M.G. Shirkoohi, R.D. Tyagi, P.A. Vanrolleghem, P. Drogui, Modelling and optimization of psychoactive pharmaceutical caffeine removal by electrochemical oxidation process: a comparative study between response surface methodology (RSM) and adaptive neuro fuzzy inference system (ANFIS), Sep. Purif. Technol. 290 (2022) 120902, https://doi.org/10.1016/j.seppur.2022.120902.
[64] I. Dalmázio, L.S. Santos, R.P. Lopes, M.N. Eberlin, R. Augusti, Advanced oxidation of caffeine in water: on-line and real-time monitoring by electrospray ionization mass spectrometry, Environ. Sci. Technol. 39 (2005) 5982–5988, https://doi.org/10.1021/es047985v.
[65] D.B. Naik, P.N. Moorthy, Studies on the transient species formed in the pulse radiolysis of benzotriazole, Radiat. Phys. Chem. 46 (1995) 353–357, https://doi.org/10.1016/0969-806X(94)00129-8.
[66] B.A. Wols, C.H.M. Hofman-Caris, Review of photochemical reaction constants of organic micropollutants required for UV advanced oxidation processes in water, Water. Res. 46 (2012) 2815–2827, https://doi.org/10.1016/j.watres.2012.03.036.
[67] T. Mohlala, T.L. Yusuf, N. Mabuba, Photoelectrocatalytic degradation of emerging organic pollutants in water on an FTO/BiVO4/NiS photoanode, J. Electroanal. Chem. 947 (2023) 117806, https://doi.org/10.1016/j.jelechem.2023.117806.
[68] T. Jiang, L. Cheng, Y. Han, J. Feng, J. Zhang, One-pot hydrothermal synthesis of Bi2O3-WO3 p-n heterojunction film for photoelectrocatalytic degradation of

norfloxacin, Sep. Purif. Technol. 238 (2020) 116428, https://doi.org/10.1016/j.seppur.2019.116428.
[69] Y. Lu, Y. Chu, W. Zheng, M. Huo, H. Huo, J. Qu, H. Yu, Y. Zhao, Significant tetracycline hydrochloride degradation and electricity generation in a visible-light-driven dual photoelectrode photocatalytic fuel cell using BiVO4/TiO2 NT photoanode and Cu2O/TiO2 NT photocathode, Electrochim. Acta 320 (2019) 134617, https://doi.org/10.1016/j.electacta.2019.134617.
[70] B.A. Koiki, B.O. Orimolade, B.N. Zwane, D. Nkosi, N. Mabuba, O.A. Arotiba, Cu2O on anodised TiO2 nanotube arrays: a heterojunction photoanode for visible light assisted electrochemical degradation of pharmaceuticals in water, Electrochim. Acta 340 (2020) 135944, https://doi.org/10.1016/j.electacta.2020.135944.
[71] G.M. Peleyeju, E.H. Umukoro, J.O. Babalola, O.A. Arotiba, Solar-light-responsive titanium-sheet-based carbon nanoparticles/B-BiVO4/WO3 photoanode for the photoelectrocatalytic degradation of orange II dye water pollutant, ACS. Omega 5 (2020) 4743–4750, https://doi.org/10.1021/acsomega.9b02148.
[72] T. Hanamorn, P. Vas-Umnuay, CFD modeling and simulation of benzyl alcohol oxidation coupled with hydrogen production in a continuous-flow photoelectrochemical reactor, Sci. Rep. 13 (2023) 22568, https://doi.org/10.1038/s41598-023-50102-7.
[73] G.C. Tedesco, P.B. Moraes, Innovative design of a continuous flow photoelectrochemical reactor: hydraulic design, CFD simulation and prototyping, J. Environ. Chem. Eng. 9 (2021) 105917, https://doi.org/10.1016/j.jece.2021.105917.
[74] D. Borrás-Jiménez, W. Silva-López, C. Nieto-Londoño, Towards the configuration of a photoelectrocatalytic reactor: part 2—Selecting photoreactor flow configuration and operating variables by a numerical approach, Nanomater. 12 (2022) 3030, https://doi.org/10.3390/nano12173030.